J. Fluid Mech. (2015), *vol.* 765, *pp.* 1–16. © Cambridge University Press 2015
doi:10.1017/jfm.2014.717

One-dimensional capillary jumps

M. Argentina[1,3,†], A. Cohen[2], Y. Bouret[2], N. Fraysse[2] and C. Raufaste[2]

[1]Université Nice Sophia Antipolis, CNRS, INLN, UMR 7335, 06560 Valbonne, France

[2]Université Nice Sophia Antipolis, CNRS, LPMC, UMR 7336, 06100 Nice, France

[3]Institut Universitaire de France, 75005 Paris, France

(Received 23 June 2014; revised 10 October 2014; accepted 9 December 2014;
first published online 15 January 2015)

In flows where the ratio of inertia to gravity varies strongly, large variations in the fluid thickness appear and hydraulic jumps arise, as depicted by Rayleigh. We report a new family of hydraulic jumps, where the capillary effects dominate the gravitational acceleration. The Bond number – which measures the importance of gravitational body forces compared to surface tension – must be small in order to observe such objects using capillarity as a driving force. For water, the typical length should be smaller than 3 mm. Nevertheless, for such small scales, solid boundaries induce viscous stresses, which dominate inertia, and capillary jumps should not be described by the inertial shock wave theory that one would deduce from Bélanger or Rayleigh for hydraulic jumps. In order to get rid of viscous shears, we consider Plateau borders, which are the microchannels defined by the merging of three films inside liquid foams, and we show that capillary jumps propagate along these deformable conduits. We derive a simple model that predicts the velocity, geometry and shape of such fronts. A strong analogy with Rayleigh's description is pointed out. In addition, we carried out experiments on a single Plateau border generated with soap films to observe and characterize these capillary jumps. Our theoretical predictions agree remarkably well with the experimental measurements.

Key words: capillary flows, foam, waves/free-surface flows

1. Introduction

Hydraulic jumps are waves that connect sections of strongly varying flows. They have been observed by famous authors, including Leonardo da Vinci, Bidone (1819), Savart (1833), Bélanger (1841) and Rayleigh (1914). The last two introduced the well-known conservation laws at the jump for mass and momentum, Rayleigh being able to derive these from a continuous description of the thickness profile. At the position of the jump, the flow speed, v, decreases drastically from supersonic to subsonic with respect to the local surface wave speed. In a thin layer of height h, the speed of gravity waves is given by $\sqrt{gh}$, where g is the acceleration due to gravity. The corresponding dimensionless number is the Froude number, $Fr = v/\sqrt{gh}$, where the velocity v is defined with respect to the reference frame where the hydraulic jump is

† Email address for correspondence: mederic.argentina@unice.fr

standing. The flow upstream of the jump, being more rapid than the surface waves, is referred to as supercritical with $Fr > 1$, while the flow downstream of the jump is referred to as subcritical with $Fr < 1$. This allows the vision of the hydraulic jump as a shock wave, in analogy with compressible gas flows (Lighthill 1978), and in which a hypothetical transition would be localized at a place where $Fr = 1$. The Mach cone, which is a characteristic of supercritical flows, has been observed in radial hydraulic jumps by Jannes *et al.* (2011), who suggested a possible transition governed by $Fr = 1$ at the jump position. In rivers, hydraulic jumps, whose position is almost stationary, appear because of variations of the river bed (Chow 1959; Simpson 1997). Tidal bores, which are wavefronts associated with a tide propagating in the opposite direction to the river current, can also be interpreted as moving hydraulic jumps (Chanson 2011). These natural objects, which share the same characteristic high Reynolds number, Re, do exhibit turbulent flows that provide strong variations of the surface profile.

In order to probe flows with moderately high Reynolds number, hydraulic jumps might be created by impacting a jet on a solid surface, as in the common operation of opening the tap of a kitchen sink. The obtained hydraulic jump takes a circular form whose radius depends on the viscosity (Watson 1964; Craik *et al.* 1981; Bohr, Putkaradze & Watanabe 1993), and is not directly given by the $Fr = 1$ criterion (applied to a hypothetical inertial flow that in fact never holds). At the centimetre scale and in this geometry, the formation mechanism appears to be a coupling between the boundary layer emerging from the solid substrate and the free surface (Watson 1964; Bowles & Smith 1992; Higuera 1994). Craik *et al.* (1981) partially observed the existence of a reverse flow, which takes the form of a toroidal vortex and acts like a springboard for the incoming fluid. This separation of the boundary layer might be explained by the existence of an adverse pressure gradient, as proposed by Kurihara (1946) and Tani (1949). Theoretical approaches (Watson 1964; Bohr, Putkaradze & Watanabe 1997; Rojas *et al.* 2010) and numerical techniques (Yokoi & Xiao 2002; Passandideh-Fard, Teymourtash & Khavari 2011) have also evidenced this peculiar flow. Various scaling laws predict a viscosity dependence for the radius position (Watson 1964; Bohr *et al.* 1997; Bush & Aristoff 2003; Rojas, Argentina & Tirapegui 2013; Duchesne, Lebon & Limat 2014). In addition, the experimental measurements of Duchesne *et al.* (2014) show the occurrence at the exit of circular hydraulic jumps of a locked value of the Froude number, whose value is independent of the flow rate imposed by the jet. One-dimensional hydraulic jumps, which have been addressed by Bonn, Andersen & Bohr (2008), are slightly different, since the upstream fluid thickness increases almost linearly in space. The hydraulic jumps created by the impact jet present the advantage of being almost laminar, but the formation mechanism appears to be also deeply linked to viscous effects.

We describe here a new kind of hydraulic jump, where the driving force has a capillary origin, gravitational effects can be omitted, and viscosity does not play a fundamental role in the formation mechanism. In a thin layer of thickness l, the characteristic surface wave velocity behaves as $\sqrt{\gamma/\rho l}$, where ρ is the density of the fluid and γ its surface tension. In such a case, the Froude number introduced in the Rayleigh theory is replaced by the Weber number $We = \rho v^2 l/\gamma$. Consequently, there exists a critical Weber number We_c below which surface waves cannot travel faster than the fluid flow. A capillary-driven hydraulic jump is expected in flows for which $We - We_c$ changes its sign. This scenario should be potentially observed in thin films falling down an inclined plane, as depicted by Kapitza (1948), in which capillary effects might dominate gravity. Nevertheless, the small length scale also introduces notable viscous shear, which affects the shock-wave criterion.

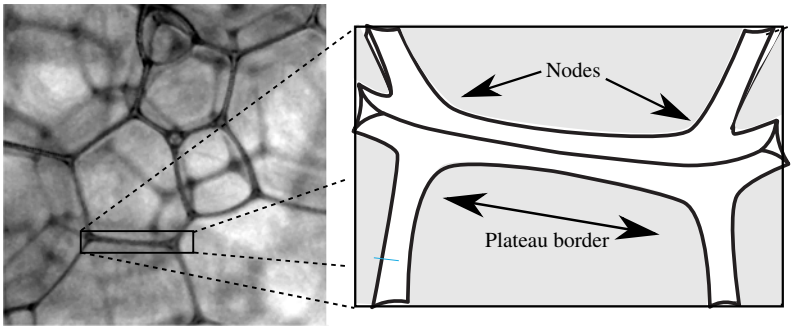

FIGURE 1. Optical photography of a liquid foam. The close-up shows a Plateau border. The grey areas represent the liquid films shared by two adjacent bubbles.

In this article, we present capillary hydraulic jumps, analogous to hydraulic jumps, formed in a Plateau border (PB). Plateau's laws describe the geometric properties of interacting soap films. At equilibrium, they always meet in threes, creating a microchannel, called a Plateau border (see figure 1). PBs merge into nodes and the PB–node network creates a porous medium that mediates the liquid flows. Usually, drainage in a gravitational field can be described using low-Reynolds-number flows in a Darcy-like approach (Weaire *et al.* 1993; Koehler, Hilgenfeldt & Stone 1999). In capillary suction experiments, flow is triggered by capillary effects due to PB thickness inhomogeneities. In that case, the Ohnesorge number $Oh = \sqrt{We}/Re$ discriminates between different regimes for fluid flow (Cohen *et al.* 2014). We have used here $Re = \rho v l/\eta$, where the fluid viscosity is η. For $Oh > 0.05$, PB perturbations disappear through viscous damping, whereas for $Oh < 0.05$, inertia dominates the flow and a wave, similar to a hydraulic jump, propagates along the PB with an almost constant velocity. This is the regime we address in this study.

This article is organized as follows. Section 2 describes a simple model for capillary jumps in PBs. The comparison between our theoretical predictions and our experimental measurements are presented in § 3. In § 4, we propose an energetic argument providing a selection mechanism for capillary jumps.

2. Model

The model aims at computing the shape and velocity of the capillary jump. We consider the Plateau border depicted in figure 2: the three holding films are attached to a triangular prism frame; the liquid flows along the z axis; and R_{ext} defines the radius of the circum-circle of the equilateral triangles defining the holding frame.

The interior region delimited by the arcs $\widehat{AB}$, $\widehat{BC}$ and $\widehat{CA}$ defines the PB channel. We assume a constant pressure P_{ext} in the surrounding air. Laplace's law predicts the radius of curvature of the arcs as $R = \gamma/(P_{ext} - P)$, such that the cross-section of the PB is symmetric, since all the surfaces of the channel share the same curvature. Here γ is the surface tension and P the pressure inside the fluid. The channel thickness $e = (\sqrt{3}/2)R$ is defined as the height of the equilateral triangle ABC. The segments AA', BB' and CC' represent the three films composed of two interfaces separating the fluid from the air.

We denote by $\mathscr{P} = \pi R$ the PB perimeter and by $\mathscr{A} = \alpha R^2$ its cross-sectional area, with $\alpha = \sqrt{3} - (\pi/2)$. The length $\mathscr{L}$ of the interfaces on the cross-section is the sum

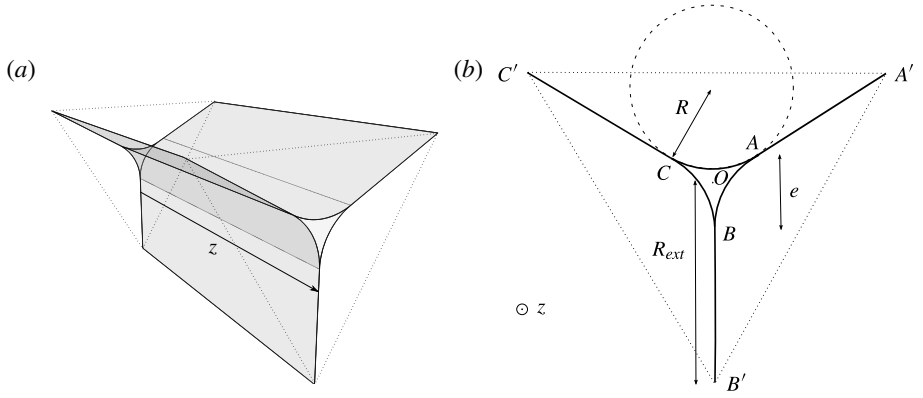

FIGURE 2. (*a*) Three-dimensional representation of the system. The grey surfaces represent the liquid–air interfaces. The dashed lines represent equilateral triangles with a circum-circle of radius R_{ext}. (*b*) Arbitrary cross-section of the system showing the Plateau border with its three holding films. The thick curves represent liquid–air interfaces. The thickness, e, of the PB is proportional to its radius of curvature, R.

of the perimeter $\mathscr{P}$ and six times the distance AA' (the factor 2 arises because each film is composed of two liquid–air interfaces):

$$\mathscr{L} = -2\alpha R + 6R_{ext}. \tag{2.1}$$

As a consequence, the area of the liquid–air interfaces of the system decreases as R increases, as pointed out by Géminard *et al.* (2004). The PB capillary energy, proportional to $\mathscr{L}$, decreases as the PB thickness e increases. From an energetic point of view, the PB tends to increase its size e, which is a necessary condition for the existence of a capillary jump.

The model derivation is based on the following assumptions.

(i) The flow is laminar and characterized by a high Reynolds number.
(ii) The pressure P and the longitudinal velocity u inside the channel depend only on z.
(iii) The variations of all the physical variables are small in the z direction.

The jump propagates with a constant velocity of amplitude c towards a region where the fluid velocity is zero and $R = R_i$. Experimentally, the injection of fluid inside the PB, initially at rest with $R = R_i$, might create the jump as the fluid excess propagates (see § 3).

The system is described in the reference frame of the capillary jump, where the flow is steady, as shown in figure 3. With the variable Z attached to the reference frame of the front ($Z = z - ct$, with z the variable in the laboratory frame), the mass conservation is written as

$$\partial_Z(u\mathscr{A}) = 0, \tag{2.2}$$

where we have neglected the mass flow inside the films, since their area in the cross-section is negligible compared to $\mathscr{A}$. We write the longitudinal momentum conservation in a slice of fluid between Z and $Z + \mathrm{d}Z$ as

$$\partial_Z[\mathscr{A}(\rho u^2 + P - P_{ext} - \sigma_{zz}) - \gamma\mathscr{L}] = 0. \tag{2.3}$$

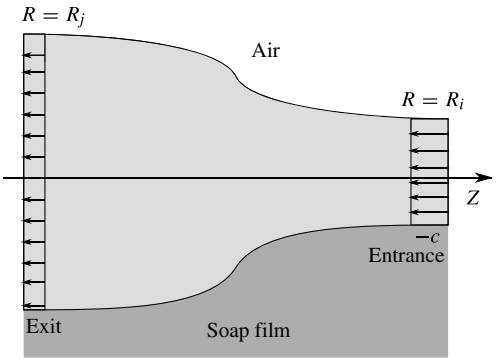

FIGURE 3. Longitudinal section of the capillary jump, in its reference frame. The jump moves to the right with a velocity c in the laboratory frame.

The first term in the momentum flux arises from the flow inside the channel. Surface tension exerts a longitudinal force proportional to $\mathscr{L}$ pointing outwards from the infinitesimal cylinder. Longitudinal flows inside the films have been neglected with respect to those inside the channel. The term $\sigma_{zz} = 2\eta\partial_Z u$ is the viscous shear stress applied to the cross-section oriented in the Z direction. The fluid pressure P, evaluated at the fluid surface, obeys the dynamic boundary condition

$$P + \gamma\kappa = P_{ext} + \sigma_{rr} \quad \text{on } \widehat{AB}, \widehat{BC}, \widehat{CA}, \tag{2.4}$$

valid in the limit of small longitudinal deformations of the interfaces. Here σ_{rr} is the normal fluid shear stress applied to the surface of the PB. The mean curvature κ can be written as

$$\kappa = \frac{1}{R(Z)} + \beta_1 R''(Z) + \beta_2 \frac{R'(Z)^2}{R(Z)}, \tag{2.5}$$

obtained in the small slope limit (see appendix A), where $\beta_{1,2}$ are geometrical coefficients. To close the model, we compute an approximation of the viscous stress $\sigma_{rr} = 2\eta\partial_r u_r$, with u_r defined as the radial velocity. The fluid is incompressible, and we relate the radial velocity with the longitudinal velocity using the divergence-free flow relation following an idea developed by Bogy (1979):

$$\frac{1}{r}\partial_r(ru_r) + \partial_Z u = 0, \tag{2.6}$$

where the angular dependence has been disregarded. Integrating this relation gives $u_r = -(r/2)\partial_Z u$. Consequently, the radial viscous stress approximates to

$$\sigma_{rr} = -\eta\partial_Z u. \tag{2.7}$$

This rough approximation gives σ_{rr} that is similar to the radial shear stress in cylindrical jets. Inserting (2.1), (2.4), (2.5) and (2.7) into (2.3) yields

$$\partial_Z \left[\mathscr{A} \left(\rho u^2 + \gamma \left(\frac{1}{R} - \beta_1 \partial_{ZZ} R - \beta_2 \frac{(\partial_Z R)^2}{R} \right) - 3\eta\partial_Z u \right) \right] = 0. \tag{2.8}$$

Note that the sign of the $1/R$ coefficient has changed with respect to the mean curvature expression (2.5), owing to the tension induced by the holding films. These

latter generate a homogeneous pressure as is the case for cylindrical jets. The equation (2.8) is integrated to give

$$\rho u^2 + \gamma \left(\frac{1}{R} - \beta_1 \partial_{ZZ} R - \beta_2 \frac{(\partial_Z R)^2}{R} \right) - 3\eta \partial_Z u = \frac{d}{R^2}, \tag{2.9}$$

where the integration constant d is determined by the boundary conditions.

Because of the Galilean invariance, we assume that, in the laboratory frame, the capillary jump propagates with a velocity c towards $z \to +\infty$, at which $R = R_i$, as shown in figure 3. The value of R at $z \to -\infty$ is denoted R_j. We summarize the boundary conditions as follows:

$$u(\infty) = -c, \tag{2.10}$$
$$R(-\infty) = R_j, \tag{2.11}$$
$$R(\infty) = R_i. \tag{2.12}$$

Using R_i and c as the characteristic length and velocity of the system, we rescale the physical quantities as $u = cv$, $R = R_i a$ and $Z = R_i s$. The set of equations (2.2) and (2.9) becomes

$$v = -\frac{1}{a^2}, \tag{2.13}$$
$$\frac{1}{a^4} - \frac{d_2}{a^2} + \frac{1}{We} \left(\frac{1}{a} - \beta_1 \partial_{ss} a - \beta_2 \frac{(\partial_s a)^2}{a} \right) - \frac{1}{Re} \frac{6}{a^3} \partial_s a = 0, \tag{2.14}$$

where d_2 is the dimensionless integration constant arising from d. We have introduced the Weber number We and the Reynolds number Re:

$$We = \frac{\rho c^2 R_i}{\gamma}, \quad Re = \frac{\rho c R_i}{\eta}. \tag{2.15a,b}$$

The capillary jump velocity c is still an unknown. Two boundary conditions fix d_2 and We. Imposing (2.12) on (2.14) settles $d_2 = 1 + (1/We)$. The boundary condition (2.11) gives the following relation:

$$We = \tilde{r}^2 \frac{1}{1 + \tilde{r}}, \tag{2.16}$$

where we have introduced the ratio $\tilde{r} = R_j/R_i$. The capillary jump velocity is deduced from (2.15*a*,*b*) and (2.16):

$$c = \sqrt{\frac{\gamma}{\rho R_i}}\, \tilde{r} \frac{1}{\sqrt{1 + \tilde{r}}}, \tag{2.17}$$

such that the propagation velocity is proportional to the capillary wave velocity $c_0 = \sqrt{\gamma/\rho R_i}$, and a geometrical factor that depends only on the ratio $\tilde{r}$. The Reynolds number defined in (2.15*a*,*b*) becomes

$$Re = \frac{1}{Oh} \frac{\tilde{r}}{\sqrt{1 + \tilde{r}}}, \tag{2.18}$$

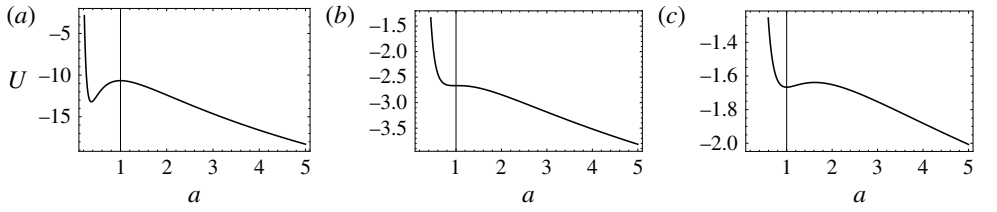

FIGURE 4. Dependence of the potential energy $\mathscr{U}$ on We: (a) $We = 0.1$; (b) $We = 1/2$; (c) $We = 1$.

where $Oh = \eta/\sqrt{\rho\gamma R_i}$ is the Ohnesorge number, which is the ratio of viscous stresses induced by capillary waves to inertia.

Equation (2.14) presents a nice analogy with the differential equations of mechanical nonlinear oscillators, since it may be written in the following form:

$$\frac{\beta_1}{We}\partial_{ss}a + f(a, Re, We)\partial_s a + \partial_a \mathscr{U} = 0. \tag{2.19}$$

The dimensionless space variable s is analogous to the temporal variable t of oscillators. As usual, the first term represents the acceleration. A dissipation function appears in factor of $\partial_s a$, i.e. $f(a, Re, We) = 6/(a^3 Re) + \beta_2(\partial_s a/aWe)$. This analogy suggests that $\mathscr{U} = 1/(3a^3) - (1 + 1/We)/a - \ln(a)/We$ stands for an effective potential energy, which is plotted in figure 4. The function $\mathscr{U}$ has one maximum and one minimum, given the physical constraint $a > 0$.

2.1. *Capillary jump*

The capillary jump is the heteroclinic trajectory that connects two extrema of $\mathscr{U}$, namely for $a(-\infty) = R_j/R_i$ and $a(\infty) = 1$. As consequence, $a = R_j/R_i$ must be the position of the maximum of U, whereas $a = 1$ must be the position of the finite minimum of $\mathscr{U}$. This last condition, $\partial_{aa}U|_{a=1} > 0$, turns into

$$We > \tfrac{1}{2}. \tag{2.20}$$

The analogy with Rayleigh theory for hydraulic jumps becomes straightforward. A capillary jump with $R_j > R_i$ exists only if $We > 1/2$, which is equivalent to the supercritical criterion $Fr > 1$ for hydraulic jumps. Owing to the oscillating nature of (2.19), undulations are expected during the relaxation of a to 1. Two numerical profiles are shown in figure 5(a). For low values of the Reynolds number, the viscous forces dominate the inertia, and a becomes monotonic. The oscillation wavelength is assessed from a linear analysis of (2.19) around $a = 1$ by studying the dynamics of a perturbation $b = a - 1$:

$$\frac{\beta_1}{We}\partial_{ss}b + \frac{6}{Re}\partial_s b + \left(2 - \frac{1}{We}\right) = 0. \tag{2.21}$$

Since this equation is linear, imposing $b \sim \mathrm{e}^{qs}$ yields

$$q = -3\frac{We}{\beta_1 Re} \pm \mathrm{i}\frac{1}{\sqrt{\beta_1}}\sqrt{2We - 1} + o\left(\frac{1}{Re}\right)^2. \tag{2.22}$$

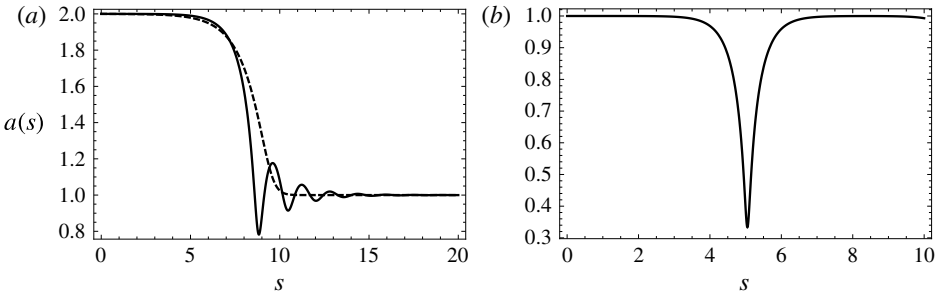

FIGURE 5. Plateau border profiles. (*a*) Capillary jumps numerically computed for $We = 4/3$ (equivalent to $\tilde{r} = 2$). Solid and dashed curves have been obtained for $Re = 60$ and $Re = 10$, respectively. (*b*) Solitary wave profile, for very low viscosities, obtained numerically from (2.24) with $We = 1/6$.

For small Reynolds number, viscosity damps oscillations, as the real part of q becomes very high. The dimensional wavelength $\lambda = 2\pi R_i/\mathrm{Im}(q)$ is

$$\lambda = R_i \frac{2\pi\sqrt{\beta_1}}{\sqrt{2We - 1}} \tag{2.23}$$

2.2. *Solitary wave*

In the case where viscous shear can be neglected, i.e. $Re \gg 1$, our model predicts the existence of solitary waves, which are homoclinic orbits connected to $a = 1$. In this parameter regime, (2.14) multiplied by $a^2\partial_s a$ and integrated with respect to the variable s reduces to

$$\frac{a(s)^2(1 - \beta a'(s)^2)}{2We} - \frac{(We + 1)a(s)}{We} - \frac{1}{a(s)} = E. \tag{2.24}$$

To derive the previous relation, we have assumed $\beta_1 = \beta_2 = \beta$, since β_1 and β_2 have almost the same numerical value (see appendix A). The boundary conditions $a(\infty) = 1$ and $a'(\infty) = 0$ fix the value $E = -(1 + 4We)/2We$. Finally, the profile minimum $a_m = 2We$ is obtained by solving (2.24) with $a'(s) = 0$. A typical spatial profile of the solitary wave is shown in figure 5(*b*); its velocity is deduced from (2.16) as

$$c = c_0\sqrt{\frac{a_m}{2}}. \tag{2.25}$$

Physically, these waves take the form of a localized constriction of the Plateau border, travelling with a constant speed. A localized perturbation yielding a localized contraction might generate two of these solitary waves travelling in opposite directions. These structures are not connected to an external reservoir, like the previously described capillary jumps.

3. Experimental study

3.1. *Materials and methods*

In order to create the Plateau border, we constructed a 15 mm long triangular-prism frame. After dipping it into a soapy solution, the PB appears in the longitudinal

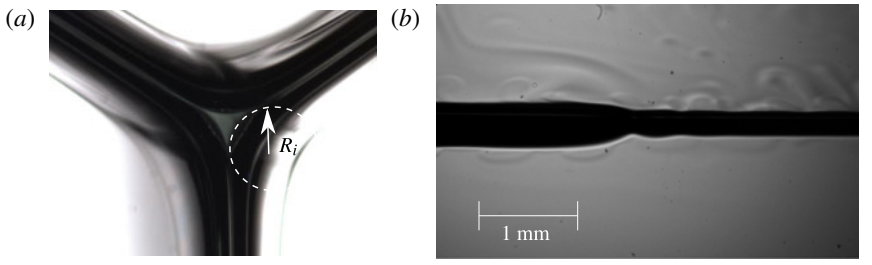

FIGURE 6. (*a*) Cross-section of the unperturbed Plateau border. Here $R_i = 0.261$ mm. (*b*) Longitudinal view of a propagating capillary jump on the Plateau border (solution I).

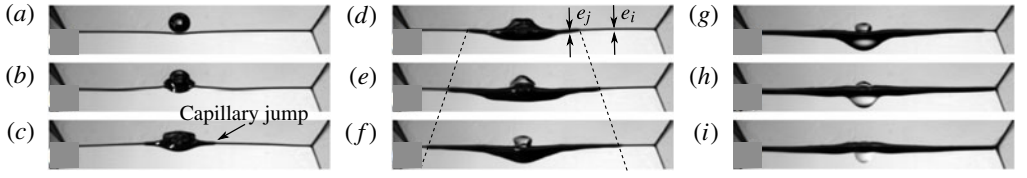

FIGURE 7. Snapshots of a Plateau border with two propagating capillary jumps. The pictures are recorded every 2.5 ms. (*a*) A droplet is released from above. (*b*) It coalesces with the PB. (*c*) Two capillary jumps are formed, one on each side of the droplet. (*d–g*) They propagate along the PB. (*h*,*i*) They reach the nodes. The two dashed lines are for guidance only, to show that a steady regime is reached.

direction. The frame is positioned to settle the PB horizontally, and rotated around its longitudinal axis such that the channel profile adopts the Y shape shown in figures 2 and 6(*a*). We can vary the radius of curvature of the PB, R_i (see figure 6*a*), by injecting liquid at one upper corner of the frame. In this study, we have used two liquid solutions leading to tangential-stress-free interfaces (Pitois, Fritz & Vignes-Adler 2005; Raufaste, Foulon & Dollet 2009).

(i) Solution I was obtained by adding 5 % of a commercial dishwashing liquid (Dreft, Procter & Gamble) to deionized water. The physical properties of solution I are $\rho = 980$ kg m^{-3}, $\gamma = 26$ mN m^{-1} and $\eta = 1.08$ mPa s.

(ii) Solution II was obtained by dissolving tetradecyl trimethyl ammonium bromide (TTAB) in deionized water. The physical properties of solution II are $\rho = 1030$ kg m^{-3}, $\gamma = 36$ mN m^{-1} and $\eta = 1.04$ mPa s.

For both solutions, the density ρ was measured by weighing a known volume of solution (error of ± 50 kg m^{-3}), the dynamic viscosity η was determined using a Ubbelohde viscometer (error of ± 2 %) and the surface tension γ was measured using the pendant drop method (error of ± 1 mN m^{-1}), as described in Hansen & Rødsrud (1991).

Experiments are backlit and recorded from the side by means of a high-speed camera (1000–2000 frames per second), in order to follow the temporal evolution of the Plateau border (figure 7). A calibration step is performed before each set of experiments, which consists in coupling cross-sectional and longitudinal views, in order to deduce the radius of curvature R of the Plateau border from its apparent thickness, e; this calibration gives $R_i = (1.08 \pm 0.02)e_i$.

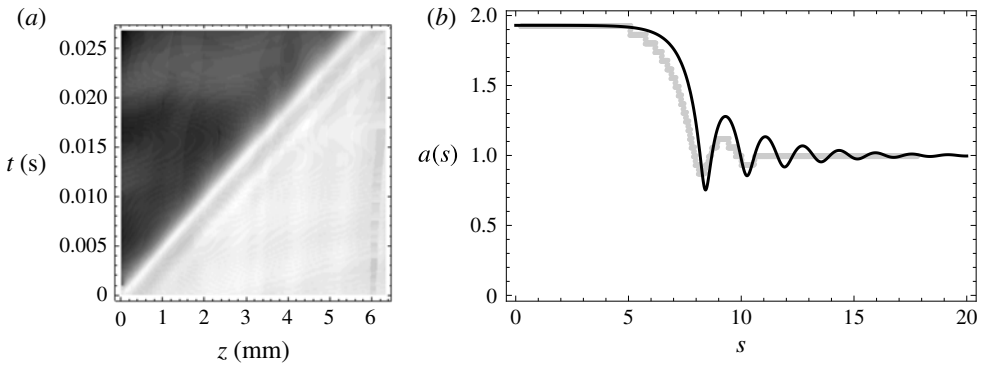

FIGURE 8. (*a*) Space–time diagram of the thickness of the capillary jump for solution I. The darkest (lightest) grey represents 0.582 mm (0.216 mm) for the thickness of the PB. (*b*) Comparison with the model of the capillary jump profile observed for solution I. Grey discs represent the experimental thickness of the PB measured optically and renormalized by the thickness e_i of the PB at the entrance. The experimental radii of curvature of the PB upstream and downstream of the jump are $R_i = 0.30$ mm and $R_j = 0.57$ mm, respectively. Equation (2.16) gives $We = 1.35$ and $Re = 95$, when computed with a velocity $c = 0.28$ m s^{-1} deduced from (2.17) and the physical values of solution I. This sets the profile $a(s)$ (black curve) predicted by (2.14).

3.2. *Experimental results and comparison with the model*

To create a capillary jump, we perturb the Plateau border by releasing a small droplet of the same surfactant solution from above, as seen in figure 7(*a*). After a transient time, a permanent regime sets in and two propagative capillary jumps are created on the two sides of the droplet, as pictured in figure 7. The droplet radius, which varies in our experiments from 0.2 to 1.8 mm, does not play a significant role in the characteristics of the capillary jumps (see Cohen *et al.* 2014). As an example, we show in supplementary movie 1 (available at http://dx.doi.org/10.1017/jfm.2014.717) a jump formation following drop coalescence at one edge of the PB. After a short transient regime, observed on a length scale given approximately by the perturbation size, these structures propagate steadily with a constant velocity, c, and exhibit small spatial oscillations near the jumps as shown in figure 6(*b*). This is illustrated by supplementary movie 2. A space–time diagram of the apparent PB thickness (figure 8*a*) demonstrates that c remains constant during the propagation. This diagram was constructed as follows. The set of pictures (one example of which is shown in figure 6*b*) extracted from a movie was binarized to discriminate the PB from the air. For each binarized picture, the liquid thickness profile is computed (one example is shown in figure 8*b*) and is associated to a grey scale. This settles the horizontal line for this given time in the space–time diagram.

3.2.1. *Capillary jump profile*

The PB profile exhibits damped spatial undulations upstream (see figure 6*b*). These wavy deformations are stationary in the reference frame of the capillary jump, as shown in the space–time diagram of the PB thickness in figure 8(*a*). To compare the experimental profile to our model, we use a Runge–Kutta method, precise at fourth order, as numerical scheme (Press *et al.* 2007). In order to compute the spatial evolution of $a(s)$, we first use the experimental values of R_i and R_j to obtain *We*

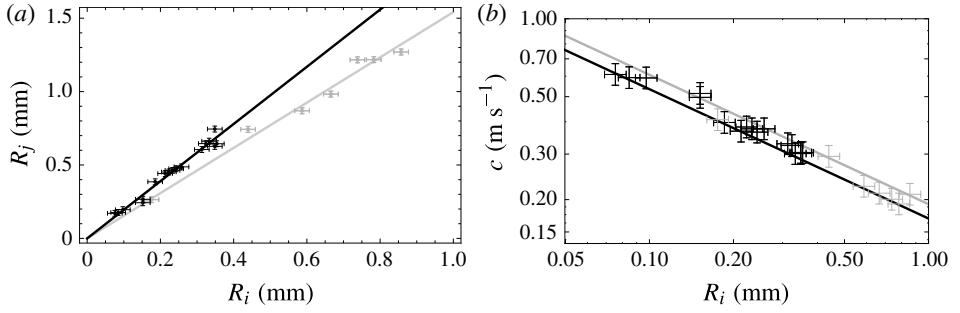

FIGURE 9. (*a*) Plot of R_j versus R_i, measured for solution I (black markers) and solution II (grey markers). The black and grey curves represent $R_j/R_i = 1.93$ and $R_j/R_i = 1.54$, respectively. (*b*) Velocity of the capillary jump as a function of R_i (logarithmic scales), measured on solution I (black markers) and solution II (grey markers). The black and grey solid lines are the velocity predictions using (2.17) for each data set.

through (2.16). The capillary jump velocity c is computed from (2.17), and used to evaluate Re. The numerical profile is then computed via a shooting method with the initial boundary conditions $a(0) = R_j/R_i$ and $a'(0) = -\epsilon$. The small parameter ϵ controls the position of the capillary jump, but does not affect the shape of $a(s)$ since (2.14) is invariant under space translation. We choose ϵ in order to superimpose the profile onto the experimental one, as can be seen in figure 8(*b*). The numerical integration of (2.14) matches very well with the experimental observation, although the model has been derived within a small slope approximation. The model nicely captures the undulations together with the typical size of the jump. The dissipation model does not accurately predict the maxima of the oscillations: a much more precise description of the shear stresses including the angular dependence has to be developed. Nevertheless, our present model already captures the fundamental physics of the capillary jump.

3.2.2. *Capillary jump aspect ratio*

In figure 9(*a*), we show the measured radius R_j of curvature of the PB downstream of the jump, for the two solutions I and II: R_j is plotted as a function of the measured initial radius of curvature of the PB, R_i. For each liquid solution, the data points coalesce onto a line. A linear regression gives $R_j = (1.93 \pm 0.03)R_i$ for solution I and $R_j = (1.54 \pm 0.03)R_i$ for solution II. For each solution, the ratio R_j to R_i appears to be constant within a good accuracy. This aspect ratio is the input parameter of our model and sets the geometrical factor of (2.17) to 1.13 and 0.96, and the Weber number of (2.16) to 1.27 and 0.92 for solutions I and II, respectively.

3.2.3. *Capillary jump velocity*

We measured the velocity of the jumps for solutions I and II. Figure 9(*b*) shows the dependence of the jump velocity on R_i. For both solutions, a linear regression of the experimental points yields a scaling with a power law -0.50 for the jump velocity. Figure 9(*b*) shows the remarkable agreement between our model prediction and the experimental measurements.

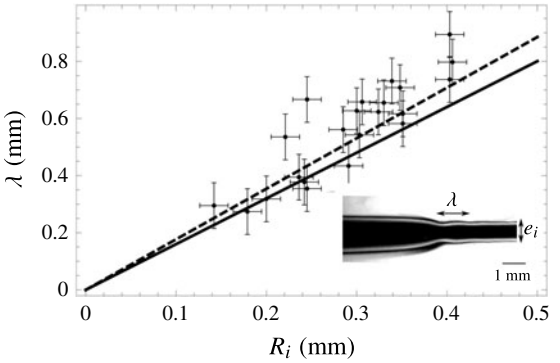

FIGURE 10. Wavelength λ versus R_i, measured on capillary jumps observed for solution I. The dashed line represents the best linear fit $\lambda = (1.78 \pm 0.1)R_i$. The continuous line $\lambda = 1.6R_i$ stands for the model prediction of equation (2.23).

3.2.4. *Upstream undulations*

As observed by Craik *et al.* (1981) in radial hydraulic jumps, capillary waves might decorate the jump rim, in the supercritical regime. The capillary jump shares this property. These steady undulations travel with the structure. We have measured the wavelength, λ, in experiments with liquid solution I, and these are reported in figure 10. The best linear fit gives $\lambda = (1.8 \pm 0.02)R_i$ whereas our model predicts $\lambda = 1.6R_i$, and slightly underestimates the experimental wavelengths.

4. Selection mechanism of the capillary jump

In all the preceding sections, the capillary jump aspect ratio R_j/R_i was required as an input parameter for the model to retrieve the experimental observations: jump profile, front velocity and undulation wavelengths. Experimentally, this aspect ratio is found to be independent of the size of the released droplet (data not shown), and thus constant for a given liquid solution. In what follows, we assume that the jump is self-adapting in shape independently of the perturbation that created it and we show that a simple energetic argument predicts the value R_j/R_i chosen by the system. The excess of energy injected at $\pm\infty$ is viscously dissipated within the whole channel. Following Landau & Lifshitz (1987), the energy balance is written as

$$\left[\mathscr{A}u\left(\frac{\rho u^2}{2} + (P - P_{ext})\right) + \gamma \mathscr{L}u\right]_{-\infty}^{\infty} = -\int_{-\infty}^{\infty}\int_{\mathscr{A}} \Phi \, \mathrm{d}\mathscr{A} \, \mathrm{d}z, \tag{4.1}$$

where Φ is the viscous dissipation per unit volume. For a Newtonian fluid, this term in cylindrical coordinates is $\Phi = \eta[2(\partial_z u)^2 + 2(u_r/r)^2 + 2(\partial_r u_r)^2 + (\partial_r u + \partial_z u_r)^2]$, which becomes $\Phi = \eta[3(\partial_z u)^2 + (R^2(\partial_{zz}u)^2)/4]$ within the approximation $r \simeq R$. In dimensionless variables, (4.1) is written as

$$\left[\frac{1}{2a^4} + \frac{1}{We}\frac{1}{a}\right]_{-\infty}^{\infty} = \frac{12}{Re} I(Oh, \tilde{r}), \tag{4.2}$$

$$I(Oh, \tilde{r}) = \int_{-\infty}^{\infty} \left(\frac{1}{a^2}\partial_s a\right)^2 + \frac{1}{48}\left(a^2 \partial_{ss}\frac{1}{a^2}\right)^2 \mathrm{d}s. \tag{4.3}$$

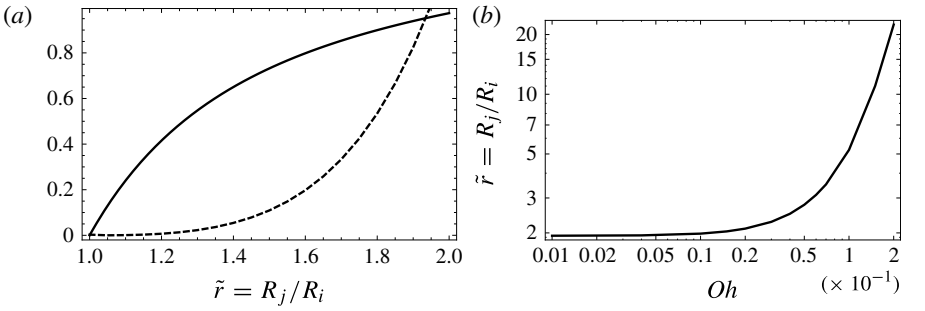

FIGURE 11. (*a*) Graphical determination of the selected ratio $\tilde{r} = R_j/R_i$ for $Oh = 10^{-3}$. The thick solid curve and the dashed curve are the left-hand side and right-hand side functions of (4.4), respectively. (*b*) Selected ratio $\tilde{r}$ as a function of the Ohnesorge number Oh.

For a given ratio R_j/R_i, the Weber number can be computed by use of (2.16), while c is predicted through (2.17).

The differential equation (2.14) is then controlled through the ratio $\tilde{r} = R_j/R_i$ and Oh. The same holds for the profile of the capillary jump and its associated integral (4.3). We reduce (4.2) to an equation for the unknown $\tilde{r}$:

$$\frac{(1+\tilde{r})^{5/2}(\tilde{r}-1)}{2\tilde{r}^3} = 12Oh\, I(Oh, \tilde{r}). \tag{4.4}$$

Solving the previous equation gives the curvature radius ratio R_j/R_i selected by the droplet-mediated jump creation. The integral (4.3) can be evaluated numerically using a simple trapezoidal integration of the profile computed with (2.14). In figure 11(*a*), we plot the left-hand side and the right-hand side of (4.4).

In figure 11(*b*), we show the dependence of the numerically computed ratio $\tilde{r}$ with respect to Oh. The R_j/R_i value tends to 1.934 for small Oh values. For liquid solutions I and II, we experimentally visited the ranges $0.01 < Oh < 0.02$ and $0.005 < Oh < 0.008$, respectively, and the values of R_j/R_i were measured to be 1.93 and 1.54, respectively. The small discrepancy can be explained by additional dissipative sources. In our model, the surface shear has been disregarded and this assumption might not be valid for all classes of surfactant, as described by Buzza, Lu & Cates (1995). Given that the predicted value is obtained by integrating over the whole PB profile, with no free parameter, the agreement is very satisfactory.

For the highest values of Oh, the selected R_j/R_i value tends to be very high. Unfortunately this regime cannot be tested experimentally since no capillary jumps were observed for $Oh \geqslant 0.05$ (Cohen *et al.* 2014). From that value of Oh, the capillary jump geometry is broken and the comparison with the model is no longer possible. We add that our model cannot predict this transition since the geometry is prescribed to that of a capillary jump.

5. Conclusion

In this article, we have reported a new kind of hydraulic jump mediated by capillary forces, instead of gravity. We have proposed a simple model for describing

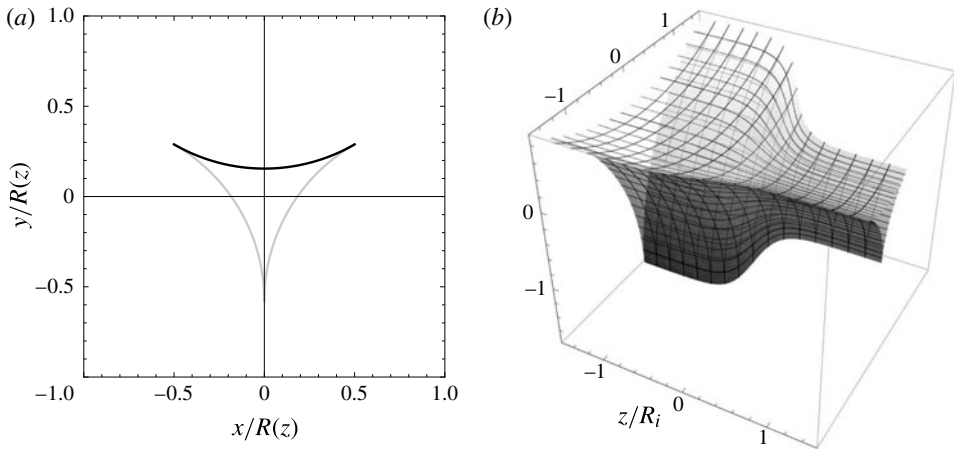

FIGURE 12. (*a*) Schematic of the cross-section of the Plateau border. The thick curves represent the liquid–air interfaces. The thick black arc is the parametrized interface defined by (A 1) and (A 2). (*b*) Three-dimensional sketch of the Plateau border defined with a hyperbolic tangent function for $R(z)$.

this hydraulic jump propagating along a Plateau border. The physics at play is controlled through the Weber and Reynolds numbers. The analogy with hydraulic jumps is evidenced by the existence condition $We > 1/2$. The propagation velocity and the profile are predicted through an equation describing the dynamics of a damped nonlinear oscillator. A simple and original experimental design has been proposed and implemented, which made the observation of these capillary jumps possible. All the measurements agree with the predictions of the theoretical approach, and confirm its validity, although we have never observed the solitary wave predicted by the model for $We < 1/2$, probably due to a too high viscosity of the liquid solutions.

Supplementary movies

Supplementary movies are available at http://dx.doi.org/10.1017/jfm.2014.717.

Appendix A

In this appendix, we compute the averaged mean curvature (i.e. the mean curvature averaged over the azimuthal coordinate for a given cross-section) of the Plateau border. In figure 12(*a*), we show the cross-section of the channel. The top interface is parametrized as an arc of a circle of radius $R(z)$,

$$x = R(z)\cos\phi, \tag{A 1}$$

$$y = R(z)(\nu - \sin\phi), \tag{A 2}$$

where $\phi \in [\pi/3, 2\pi/3]$ and $\nu = 2/\sqrt{3}$. The diagonalization of the Hessian matrix on this surface yields the mean curvature

$$H_g = -\frac{R(z)(1-\nu\sin\phi)R''(z) - (-2\nu\sin\phi + \nu^2 + 1)R'(z)^2 - 1}{R(z)[(\nu\sin\phi - 1)^2 R'(z)^2 + 1]^{3/2}}. \tag{A 3}$$

Clearly, the variation of $R(z)$ induces a dependence of the curvature on the angular variable, as evidenced in figure 12(*b*). This expression simplifies to

$$H_g = \frac{1}{R(z)} + \frac{1}{3}[(3+2\sqrt{3})\sin\phi - 3]R''(z) \tag{A 4}$$

$$+ \frac{[-3(7+4\sqrt{3})\sin^2\phi + (6+4\sqrt{3})\sin\phi + 8\sqrt{3}+11]R'(z)^2}{6R(z)} + \text{h.o.t.}, \tag{A 5}$$

in the small slope limit. Since the model assumes no angular dependence, we average this relation between $\phi = \pi/3$ and $\phi = 2\pi/3$ and we finally get the averaged mean curvature within the small slope approximation:

$$\kappa = \frac{1}{R(z)} + \beta_1 R''(z) + \beta_2 \frac{R'(z)^2}{R(z)}, \tag{A 6}$$

where $\beta_1 = (2\sqrt{3}-\pi)/\pi \sim 0.103$ and $\beta_2 = (3\sqrt{3}-\pi)/6\pi \sim 0.109$.

REFERENCES

Bélanger, J. B. 1841 Notes sur l'hydraulique, Ecole Royale des Ponts et Chaussées, Paris, France, session 1842, p. 223.

Bidone, G. 1819 Le remou et sur la propagation des ondes. *Rep. R. Sci. Acad. Turin* **12**, 21–112.

Bogy, D. B. 1979 Drop formation in a circular liquid jet. *Annu. Rev. Fluid Mech.* **11**, 207–228.

Bohr, T., Putkaradze, V. & Watanabe, S. 1993 Shallow-water approach to the circular hydraulic jump. *J. Fluid Mech.* **254**, 635–648.

Bohr, T., Putkaradze, V. & Watanabe, S. 1997 Averaging theory for the structure of hydraulic jumps and separation in laminar free-surface flow. *Phys. Rev. Lett.* **79**, 1038–1041.

Bonn, D., Andersen, A. & Bohr, T. 2008 Hydraulic jumps in a channel. *J. Fluid Mech.* **618**, 71–87.

Bowles, R. I. & Smith, F. T. 1992 The standing hydraulic jump: theory, computations and comparisons with experiments. *J. Fluid Mech.* **242**, 145–168.

Bush, J. W. N. & Aristoff, J. M. 2003 The influence of surface tension on the circular hydraulic jump. *J. Fluid Mech.* **489**, 229–238.

Buzza, D. M. A., Lu, C. Y. D. & Cates, M. E. 1995 Drop formation in a circular liquid jet. *J. Phys. II France* **5**, 37–52.

Chanson, H. 2011 *Tidal Bores, Aegir, Eagre, Mascaret, Pororoca. Theory and Observations*. World Scientific.

Chow, V. T. 1959 *Open Channel Hydraulics*. McGraw-Hill.

Cohen, A., Fraysse, N., Rajchenbach, J., Argentina, M., Bouret, Y. & Raufaste, C. 2014 Inertial mass transport and capillary hydraulic jump in a liquid foam microchannel. *Phys. Rev. Lett.* **112**, 218303.

Craik, A. D. D., Latham, R. C., Fawkes, M. J. & Gribbon, P. W. F. 1981 The circular hydraulic jump. *J. Fluid Mech.* **112**, 347–362.

Duchesne, A., Lebon, L. & Limat, L. 2014 Constant Froude number in a circular hydraulic jump and its implication on the jump radius selection. *Europhys. Lett.* **107** (5), 54002.

Géminard, J.-C., Zywocinski, A., Caillier, F. & Oswald, P. 2004 Observation of negative line tensions from Plateau border regions in dry foam films. *Phil. Mag. Lett.* **84**, 199–204.

Hansen, F. K. & Rødsrud, G. 1991 Surface tension by pendant drop: I. A fast standard instrument using computer image analysis. *J. Colloid Interface Sci.* **141**, 1–9.

Higuera, F. J. 1994 The hydraulic jump in a viscous laminar flow. *J. Fluid Mech.* **274**, 69–92.

Jannes, G., Piquet, R., Maissa, P., Mathis, C. & Rousseaux, G. 2011 Experimental demonstration of the supersonic–subsonic bifurcation in the circular jump: a hydrodynamic white hole. *Phys. Rev.* E **83**, 056312.

KAPITZA, P. L. 1948 Wave flow of thin viscous fluid layers. *Zh. Eksp. Teor. Fiz.* **18**, 3–28 (translation: 1965 *Collected Works of P. L. Kapitza* (ed. D. ter Haar). Pergamon).

KOEHLER, S. A., HILGENFELDT, S. & STONE, H. 1999 Liquid flow through aqueous foams: the node-dominated foam drainage equation. *Phys. Rev. Lett.* **82**, 4232–4235.

KURIHARA, M. 1946 On hydraulic jumps. In *Proceedings of the Report of the Research Institute for Fluid Engineering*, Kyusyu Imperial University **3** (2), 11–33.

LANDAU, L. D. & LIFSHITZ, E. M. 1987 *Fluid Mechanics*. Pergamon.

LIGHTHILL, J. 1978 *Waves in Fluids*. Cambridge University Press.

PASSANDIDEH-FARD, M., TEYMOURTASH, A. R. & KHAVARI, M. 2011 Numerical study of circular hydraulic jump using volume-of-fluid method. *J. Fluids Eng.* **133**, 011401.

PITOIS, O., FRITZ, C. & VIGNES-ADLER, M. 2005 Hydrodynamic resistance of a single foam channel. *Colloids Surf.* A **261**, 109–114.

PRESS, W. H., TEUKOLSKY, S. A., VETTERLING, W. T. & FLANNERY, B. P. 2007 *Numerical Recipes: The Art of Scientific Computing*, 3rd edn. Cambridge University Press.

RAUFASTE, C., FOULON, A. & DOLLET, B. 2009 Dissipation in quasi-two-dimensional flowing foams. *Phys. Fluids* **21**, 053102.

RAYLEIGH, LORD 1914 On the theory of long waves and bores. *Proc. R. Soc. Lond.* A **5**, 324–328.

ROJAS, N., ARGENTINA, M., CERDA, E. & TIRAPEGUI, E. 2010 Inertial lubrication theory. *Phys. Rev. Lett.* **104**, 18780.

ROJAS, N., ARGENTINA, M. & TIRAPEGUI, E. 2013 A progressive correction to the circular hydraulic jump scaling. *Phys. Fluids* **25**, 042105.

SAVART, F. 1833 Mémoire sur le choc d'une veine liquide lancée contre un plan circulaire. *Ann. Chim.* **54**, 56–87.

SIMPSON, J. E. 1997 *Gravity Currents: In the Environment and the Laboratory*, 2nd edn. Cambridge University Press.

TANI, I. 1949 Water jump in the boundary layer. *J. Phys. Soc. Japan* **4**, 212–215.

WATSON, E. J. 1964 The radial spread of a liquid jet over a horizontal plane. *J. Fluid Mech.* **20**, 481–499.

WEAIRE, D., PITTET, N., HUTZLER, S. & PARDAL, D. 1993 Steady-state drainage of an aqueous foam. *Phys. Rev. Lett.* **71**, 2670–2673.

YOKOI, K. & XIAO, F. 2002 Mechanism of structure formation in circular hydraulic jumps: numerical studies of strongly deformed free-surface shallow flows. *Physica* D **161**, 202–219.